Drag coefficient for a sedimenting and rotating sphere in a viscoelastic fluid

Alfonso Castillo,[1,2] William L. Murch,[3] Jonas Einarsson,[3] Baltasar Mena,[4]
Eric S. G. Shaqfeh,[3] and Roberto Zenit[2,*]

[1]*Departamento de Ingeniería Química, Facultad de Química, Universidad Nacional Autónoma de México, Ciudad de México, 04510, México*

[2]*Instituto de Investigaciones en Materiales, Universidad Nacional Autónoma de México, Ciudad de México, 04510, México*

[3]*Department of Chemical Engineering, Stanford University, Stanford, California 94305, USA*

[4]*Instituto de Ingeniería, Universidad Nacional Autónoma de México, Ciudad de México, 04510, México*

(Received 5 February 2019; published 7 June 2019)

In this work, we study the effect of sphere rotation on the drag coefficient experienced by a sphere sedimenting through a nearly constant viscosity and elastic Boger fluid, using experiments, numerical simulations, and an asymptotic theory. For the purely sedimenting (nonrotating) sphere, we find that the drag coefficient is larger in the Boger fluid than in the Newtonian case, in accordance with previous studies. In the Boger fluid, rotation of the sphere (around the axis aligned with translation) causes a reduction in the drag coefficient compared to the purely sedimenting case; this trend is observed in the experiments, numerical simulations, and theory. The numerical results indicate that the decrease in the drag due to sphere rotation results from modifications in the pressure contribution to the drag.

DOI: 10.1103/PhysRevFluids.4.063302

I. INTRODUCTION

The sedimentation of a single sphere in a viscous fluid is a classical problem in fluid mechanics. Due to its fundamental importance and practical relevance, it has been vastly studied, both for Newtonian and non-Newtonian liquids. For a rigid sphere settling in an unbounded Newtonian fluid in the creeping flow regime, the sedimentation velocity is related to the applied force on the sphere as $F_i = 6\pi\eta a U_i$, where F_i is the applied force, η is the viscosity, a is the particle radius, and U_i is the terminal settling velocity. This linear relationship, the well-known Stokes law, forms the basis for falling ball viscometry in viscous fluids.

For sedimentation studies, the fluid-sphere interaction gives rise to a characteristic deformation rate over the sphere, given by U/a, where $U = |U_i|$. In non-Newtonian fluids with viscoelasticity, one can define a dimensionless sedimentation Deborah number, De, which relates a characteristic fluid relaxation time, λ, to the characteristic deformation rate as $\mathrm{De} = \lambda U/a$. To test the effect of non-Newtonian properties on the sedimentation behavior involves the use of spheres of different size and density to cover a significant range of deformation rate, or Deborah number. Many studies have been conducted to evaluate how the drag on a sphere changes as the flow strength increases (i.e., at increasing De), as has been reviewed by McKinley [1], Caswell *et al.* [2], and Chhabra [3].

Despite many studies, the case in which the sphere simply sediments in a viscoelastic fluid is still not fully understood. The more recent reviews by D'Avino and Maffettone [4] and Zenit and Feng [5] provide good summaries of the current state of the subject. As discussed by McKinley

*zenit@unam.mx

[1], significant work has gone toward understanding whether the drag coefficient should increase or decrease (with respect to the Newtonian case) at a given Deborah number. Part of the difficulty arises because the flow kinematics for flow past the sphere are a complex mixture of both shear- and extensional-dominated flow, which can contribute differently to the drag depending on the fluid properties, sphere confinement, and flow strength [1].

An experimental investigation that further exemplifies these complexities is that by Jones *et al.* [6]. They studied the sedimentation of solid spheres in two Boger-type fluids [7,8], named Type-I (maltose syrup/water-based) and Type-II (polybutene-based). The rheological properties show that both viscoelastic fluids exhibited nearly constant shear viscosity over a reasonable range of shear rates, followed by slight shear-thinning at high shear rates. The results showed a significant drag enhancement for fluid Type-I but a slight reduction for fluid Type-II for small Deborah numbers (less than unity), followed by a drag increase in both fluids at higher Deborah number. Interestingly, other studies have described opposite trends at small Deborah number for seemingly similar fluids, with results showing a slight drag reduction for Type-I fluids and a drag increase for Type-II fluids for $\mathrm{De} < 1$ [9], which the authors suggested could be attributable to solvent quality differences. More recent work has confirmed the importance of solvent quality, polymer molecular weight, and polymer extensibility on the drag experienced by a sedimenting sphere, as elucidated by Solomon and Muller [10]. For larger Deborah number (greater than unity), where significant extension of the polymer can occur in the wake of the sphere, it has been shown that the drag on the sphere generally increases in Boger fluids [6,10–13], as summarized by Chhabra [3].

Alternatively, a nontranslating, rotating sphere has been investigated by a number of authors as a tool to evaluate rheological properties of viscoelastic fluids, as reviewed by Walters [14] and Chhabra [15]. From the measured torque on the rotating sphere and the observed flow streamlines around the sphere, the viscosity and other viscoelastic model parameters (e.g., material parameters for a second-order fluid) can be calculated [16–26]. Analysis of the secondary flow patterns can be used to calculate a combination of the normal stress differences [27,28]. The secondary flows, which result as a competition between elastic and inertial effects, were originally predicted by Thomas and Walters [18] and observed experimentally by Walters and Savins [27] and Giesekus [19,29]. These secondary flows were recently reproduced computationally and interpreted by Garduño *et al.* [30–32]. Other authors have studied how the presence of these secondary flows due to rotation in viscoelastic fluids can result in net motion (or propulsion) for two spheres with different radii [33].

This study focuses on the coupling of these two flows, i.e., for a rotating and sedimenting sphere in a viscoelastic fluid. This problem was first addressed by Giesekus, who solved for the drag and torque experienced by a rotating and translating sphere in a viscoelastic fluid modeled as a third-order fluid [34]. From the sphere's angular rotation speed, ω, a second characteristic deformation rate arises, and one can define a dimensionless rotational Weissenberg number, $\mathrm{Wi} = \lambda\omega$. Giesekus [34] predicted that in the absence of fluid inertia and in the limit of small Deborah and Weissenberg number, a rotation imposed around the axis of translation would reduce the drag on the sphere at $O(\mathrm{Wi}^2)$. Bhatnagar [35] investigated how the streamlines for uniform flow past a rotating sphere would change in a viscoelastic fluid, showing that a region of flow reversal could form at high enough rotation rates, but did not study the effect of rotation on the drag.

Recently, Godinez *et al.* [36] proposed this idea—a combination of sphere rotation and translation—to study the sedimentation of spheres in shear-thinning power law fluids. They studied spheres that were rotated using a magnetic field while sedimenting due to gravity (with the rotation axis aligned with gravity). In doing so, the flow around the sphere became dominated by the rotation of the sphere, reducing the local fluid viscosity, and the sedimentation velocity increased. From the experimental measurements of the sphere's terminal velocity, the properties of the fluid, such as the flow consistency and power index parameters, could be deduced. Hence, for a shear-thinning power-law fluid, this system could be used as a viscometer, as predicted by Bourne [37]. The present paper is a natural continuation to the work of Godinez *et al.* [36], using instead a viscoelastic fluid that exhibits nearly constant viscosity over a wide range of shear rates (the so-called Boger fluid

[7,8]). The goal of this study is to understand how the sphere rotation in a viscoelastic fluid affects the sphere's settling rate.

A similar problem, where an external shear flow was imposed in the plane perpendicular to gravity while a particle settled through the fluid, has been studied experimentally [38], theoretically [39,40], and numerically [41–43]. In this coupled flow field, the sedimentation flow around the sphere was modified by the action of an externally imposed shear in the viscoelastic fluid, resulting in a change in the drag. The experiments, theory, and simulations showed that a sphere settling in a cross sheared Boger fluid experiences a significant increase in the drag. In viscoelastic fluids that exhibit both fluid elasticity and a shear thinning viscosity, the fluid elasticity and shear-thinning viscosity can compete in a cross shearing flow to dictate whether the total drag on the sphere (when calculated based on the zero-shear viscosity) is overall increased or decreased as the cross shear rate increases [42]. In this study, rather than a sphere freely rotating in an external flow, a torque is imposed on the sphere in an otherwise quiescent fluid, and we investigate how this imposed rotation of the sphere affects the flow past the sphere.

The present investigation aims to examine the impact of rotation on the terminal velocity and therefore on the drag coefficient. We conduct both experiments and numerical simulations. The simulations are complemented and compared with a theory valid for weakly elastic fluids. The experimental fluids and apparatus are discussed in Secs. II A and II B and the numerical simulations and theory are described in Sec. III. Results from experiments are discussed in Sec. IV and results from the theory and simulations are presented in Sec. V. Conclusions and future work are discussed in Sec. VI.

II. TEST FLUIDS AND EXPERIMENTAL SETUP

A. Test fluids

The Boger fluid (BF) was chosen as a model fluid because it has a nearly constant viscosity combined with high elasticity over a range of relevant shear rates. In this manner, changes in the sedimenting speed can be attributed solely to the viscoelastic nature of the fluid. It was fabricated by dissolving polyacrylamide (PAA, molecular weight 5×10^6 g/mol) in nonionic water with slow mixing for 24 h. Afterwards, the polymeric solution was added to a glucose solution and it was slowly mixed over four days. The mass proportions were 84.96% glucose, 15% water, and 0.04% PAA. The solution was left standing for two weeks previous to testing, and residual bubbles were extracted before the test. A Newtonian reference fluid (NF) was fabricated by adding water to glucose until the fluid had similar viscosity to that of the viscoelastic fluid. It was used for testing 24 h after preparation. All fluids were stored and used in closed containers to avoid free surface crystallization.

1. Fluid characterization

The rheological characterization was performed using an Anton Paar shear rate and shear stress-controlled rheometer with a cone-plate geometry, which was used to obtain the viscosity and first normal stress difference flow curves, within the shear rate range of 1 to 100 s^{-1} at 23 °C.

Results of steady shear measurements are plotted on Fig. 1. The range of shear rates corresponding to sedimenting experiments are within the rheological measurements, as shown by the vertical dashed lines. The Boger fluid showed a nearly constant viscosity for shear rates of up to 18.1 s^{-1} followed by slight shear-thickening. The viscosity of the Boger fluid was fit to a power law model, leading to a value of the power law index $n = 0.963$. Therefore, we consider the viscosity to be effectively constant. The Newtonian fluid showed a constant viscosity with a value very close to that of the Boger fluid. The physical properties of the two fluids are summarized in Table I. The determination of the fluid relaxation time, λ_{N_1}, is discussed in Sec. II A 2.

2. Fitting rheological data to a rheological model

The Oldroyd-B model has been used with some success to model the behavior of Boger fluids [44] as it predicts a steady shear rate viscosity and a first normal stress coefficient that are

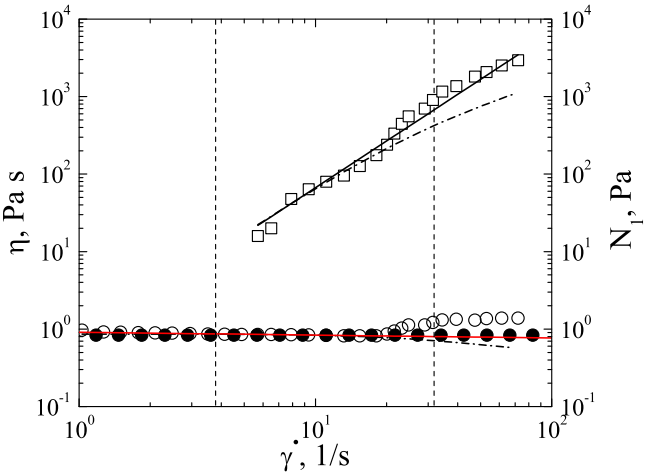

FIG. 1. Results of steady shear rheometry for the Boger fluid (empty circles) and the Newtonian fluid (filled circles). The red line shows a fit to power-law viscosity model with $m = 0.9106$ Pa s and $n = 0.963$ for $\dot{\gamma} < 20\ \mathrm{s}^{-1}$. Also, the first normal stress difference (N_1) is shown as a function of shear rate (empty squares). The Oldroyd-B (black solid line) and the FENE-P (black dashed-dotted line) models were used to fit η_0 and N_1 of the viscoelastic fluid. The full range of shear rates present in the falling rotating sphere experiments is shown with vertical dashed lines.

independent of shear rate. Physically, the Oldroyd-B model represents the polymeric solution as a dilute suspension of elastic dumbbells in a Newtonian solvent.

Following the classical treatment of this model [45,46], and considering a Newtonian solvent, in steady shear flow the first and second normal stress differences can be written as

$$N_1 = 2\eta_0(1-\beta)\lambda\dot{\gamma}^2 \tag{1}$$

and

$$N_2 = 0. \tag{2}$$

The zero-shear viscosity is $\eta_0 = \eta_p + \eta_s$, where η_p and η_s are the polymer and solvent viscosities, respectively. The ratio $\beta = \eta_s/\eta_0$ is the solvent contribution to the viscosity, and λ is the relaxation time.

Therefore, from the rheological data shown in Fig. 1, the measurement of N_1 as a function of $\dot{\gamma}$ can be fit to infer the relaxation time, $\lambda = \lambda_{N_1}$, for a known value of β. Table II shows the fitted results for the Oldroyd-B model from the data on Fig. 1.

Also shown in Fig. 1 is a fit to the shear rheology data using the FENE-P model. The FENE-P model was used in our numerical simulations to compare with the experiments. The choice of the FENE-P model is discussed in Sec. III A, and the fitting of the model, as well as the simulation results, are discussed in Sec. V B.

TABLE I. Characterization of the test fluids at 23 °C.

Solution	ρ_f, kg/m^3	n	η_0, Pa s	λ_{N_1}, s
Newtonian	1510	1	0.84	0
Boger	1508	0.963	0.8444	0.5102

TABLE II. Parameters of the Oldroyd-B model.

η_0, Pa s	η_s, Pa s	η_p, Pa s	β	λ, s
0.8444	0.1902	0.6542	0.2252	0.5102

B. Experimental setup

Experiments were performed in the device shown in Fig. 2. This setup comprises a rectangular container of 120 mm height and 100 mm width which has the fluid used and wherein the spheres are released by a special mechanism to avoid surface and inertial effects. Plastic spheres with one or more small rare Earth rod magnets (Magcraft, model NSN0658) with horizontal orientation were used. Diameters were measured by using a digital Vernier caliper. The physical properties of the spheres are shown in Table III.

Spheres were positioned below the free surface of the test fluid and left to descend by a mechanical device made of two holders which places the sphere in the center of the container filled with the test fluid. The container is placed in the middle of the device designed by [47], which produces a uniform rotating magnetic field. It is a Helmholtz coil (a pair of identical circular magnetic coils that are placed symmetrically along a common axis) that is mechanically rotated by a DC motor. Due to its size and design (coil diameter of 280 mm, with 230 turns of wire), the device is capable of producing a magnetic field of constant strength (close to 6 mT in a region of 12 cm^3 in size).

Once the sphere is released, the magnetic device is started at a previously set frequency of rotation, thus rotating the sphere along an axis parallel to gravity (aligned with sedimentation). The experimental value of the speed of sedimentation was obtained from the displacement of the sphere in consecutive frames in the imaging system named Tracker.

III. NUMERICAL SIMULATIONS AND THEORY

We complement the experimental study with numerical simulations and an asymptotic theory of the same system. We consider the terminal velocity of a sphere freely sedimenting through a

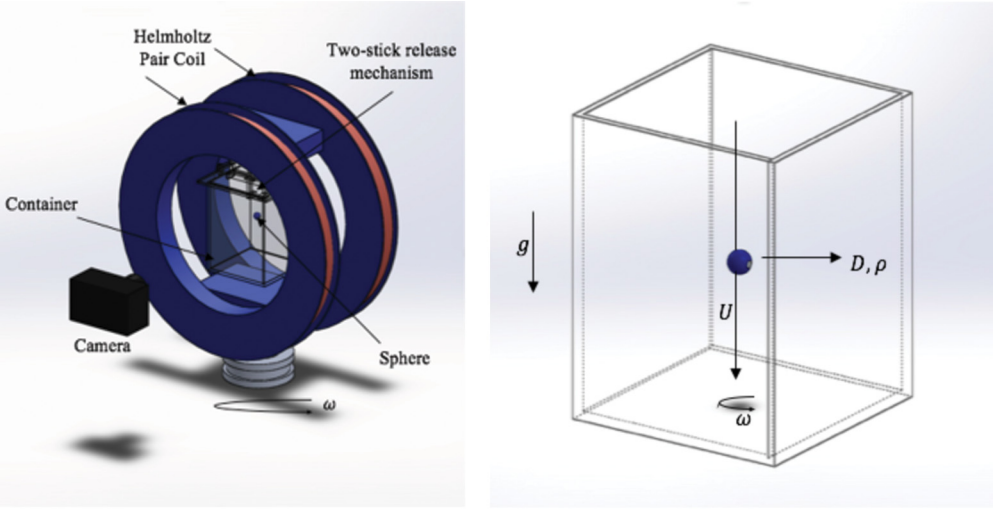

(a) (b)

FIG. 2. (a) Experimental setup; (b) container and sphere.

TABLE III. Spheres dimensions and properties.

Diameter, mm	Mass, mg	Density, kg/m^3
7.99	585	2190.37
8.72	760	2189.10
8.81	819	2287.48
9.57	1005	2189.94

quiescent viscoelastic fluid with an imposed rotation rate. In the experiments, this is achieved by imposing a strong rotating magnetic field on a freely sedimenting sphere, thus imposing a torque on the sphere sufficient to rotate the sphere at a specified rotation rate. In our simulations, we consider a nearly equivalent problem, but with a directly imposed angular velocity on the sphere, and in a reference frame translating with the sphere. These two setups allow for a direct comparison between the experiments and numerical simulations. The governing equations of motion for the viscoelastic fluid flow are described, including the choice of a constitutive model in our simulations, in Sec. III A. We discuss the boundary conditions, as well as the computational mesh used, in Sec. III B. In Sec. III C, we describe an asymptotic theory valid for weak elastic flow past a rotating sphere.

A. Governing equations

We solve the continuity and momentum equations for the flow of an incompressible fluid, including contributions to the fluid stress from the viscoelastic or polymeric components of the fluid. The governing equations can be written in dimensionless form for Cartesian coordinates, where $x_i = (x_1, x_2, x_3) = (x, y, z)$, as

$$\frac{\partial u_i}{\partial x_i} = 0, \tag{3}$$

$$\mathrm{Re}_a\left(\frac{\partial u_i}{\partial t} + u_j\frac{\partial u_i}{\partial x_j}\right) = \frac{\partial \sigma_{ij}}{\partial x_j}, \tag{4}$$

$$\sigma_{ij} = -p\delta_{ij} + \beta\left(\frac{\partial u_i}{\partial x_j} + \frac{\partial u_j}{\partial x_i}\right) + \sigma^P_{ij}. \tag{5}$$

In the above equations, u_i is the fluid velocity, p is pressure, σ_{ij} is the total fluid stress, and σ^P_{ij} is the stress contribution due to the polymers. The variables have been nondimensionalized by a characteristic length (a), characteristic velocity (U, the sphere terminal settling speed), characteristic time (a/U), and characteristic stress ($\eta_0 U/a$). We define a Reynolds number, for Eq. (4) only, as $\mathrm{Re}_a = \rho_f U a/\eta_0$. Later, in Sec. IV, Eq. (12), we will redefine the Reynolds number as $\mathrm{Re} = \rho_f U(2a)/\eta_0$, to be consistent with prior settling sphere literature.

To model the polymeric stress, σ^P_{ij}, we use two constitutive models in this study: the Oldroyd-B model and the FENE-P model (finitely extensible nonlinear elastic model with Peterlin closure). Both models represent the polymeric solution as a dilute suspension of elastic dumbbells: In the Oldroyd-B model, the dumbbell is represented as a Hookean spring, whereas in the FENE-P model, the dumbbell is represented as a finitely extensible nonlinear spring. From kinetic theory, the equations that determine the polymeric stress can be written as [45,46,48]

$$\sigma^P_{ij} = \frac{(1-\beta)}{\mathrm{De}}\left(\frac{c_{ij}}{\psi} - \delta_{ij}\right), \tag{6}$$

$$\frac{\partial c_{ij}}{\partial t} + u_k\frac{\partial c_{ij}}{\partial x_k} - c_{ik}\frac{\partial u_j}{\partial x_k} - c_{kj}\frac{\partial u_i}{\partial x_k} = -\frac{1}{\mathrm{De}}\left(\frac{c_{ij}}{\psi} - \delta_{ij}\right), \tag{7}$$

where c_{ij} is the polymer conformation tensor, ψ is a characteristic spring stiffening function, and the Deborah number has been defined as $\mathrm{De} = \lambda U/a$. The polymer conformation tensor is defined as $c_{ij} = \langle R_i R_j \rangle$, where R_i is the end-to-end vector of the polymer dumbbell, nondimensionalized by the equilibrium Hookean spring length. For the Oldroyd-B model, $\psi = 1$. For the FENE-P model,

$$\psi = \left(1 - \frac{c_{ii}}{L^2}\right), \tag{8}$$

where L is the maximum polymer extensibility parameter, also made dimensionless with the equilibrium Hookean spring length. Note that in the limit as $L^2 \to \infty$, we recover the Oldroyd-B constitutive equation.

In this study, we use the Oldroyd-B model to describe the polymeric stress in the weak flow limit, e.g., for the asymptotic theory (described in Sec. III C). For the simulation comparisons to the experiments, where the flow strength is strong [i.e., De, $\mathrm{Wi} \sim O(1)$], we use the FENE-P model to describe the polymeric stress. Numerically, the FENE-P constitutive model is useful in scenarios with high rates of deformation, as the polymer conformation tensor and the polymer stress remain bounded [49,50].

Although the FENE-P dumbbell model captures the qualitative behavior of polymer chains in steady motion, we do not expect this constitutive model to be able to quantitatively predict hydrodynamic quantities, such as the drag on a sphere, for strong flows of polymeric fluids. In the case of flow past a sphere in a polymeric viscoelastic fluid, significant work has been done to understand how the drag on a sphere changes as a function of the flow strength past the sphere (i.e., as a function of De) [1–3], and dumbbell models have had only limited success in quantitatively predicting the drag on a sphere when judged across a wide range of geometric parameters, flow conditions, and fluid types. More recently, it has been shown that a multiscale approach [51] or the inclusion of dissipative stress contributions [52] can improve the quantitative description of the drag. This is likely due to an improved description of the transient extensional viscosity of the fluids at high extension rates, which can become important for strong viscoelastic flows past a sphere [1,51]. This level of quantitative prediction for the drag on a purely sedimenting sphere was not the focus of this study. In this work, we aim to use our simulation method to qualitatively describe the effect of rotation on the drag on a spherical particle in a viscoelastic fluid, and to look for insight into the physical mechanism for why the drag may change due to an imposed rotation of the sphere.

The schematic of the simulation is shown in Fig. 3. Simulations were performed in a frame of reference translating (but not rotating) with the sphere. The boundary conditions were set accordingly for flow past a rotating sphere. Specifically, at the inlet boundary, the dimensionless velocity was set as $u_i = (u_x, u_y, u_z) = (0, 0, 1)$, and the conformation tensor was set as $c_{ij} = \delta_{ij}$. At the container walls, $u_i = (0, 0, 1)$, and a no-flux condition was used for the conformation tensor, $\partial c_{ij}/\partial n = 0$. A convective outlet boundary condition was used for both u_i and c_{ij} at the outflow boundary, i.e., $\partial\phi/\partial t + \bar{u}_z \partial\phi/\partial z = 0$, where ϕ is a velocity or conformation tensor component and $\bar{u}_z$ is the space-averaged outflow velocity. On the sphere surface, a no-slip, no-penetration velocity condition for a sphere rotating about the z axis was imposed as $u_i = (-\alpha y, \alpha x, 0)$, where $\alpha = \mathrm{Wi}/\mathrm{De} = \omega a/U$ and ω is the angular rotation speed. On the sphere surface, a no-flux condition was used for the conformation tensor.

B. Numerical setup

The simulations were performed using a parallelized three-dimensional code based on an unstructured finite volume formulation for incompressible flow. The details of the solver, as well as extensive validation tests and experimental comparisons, can be found in prior studies [41–43,49,53,54]. The schematic of the simulation is shown in Fig. 3. The domain mesh was a boundary-fitted mesh and did not move or stretch during the simulation. An unstructured tetrahedral discretization of the domain shown in Fig. 3 was used for all simulations. It should be noted that if we were to assume axisymmetry around the rotation axis, this problem could be reformulated in two

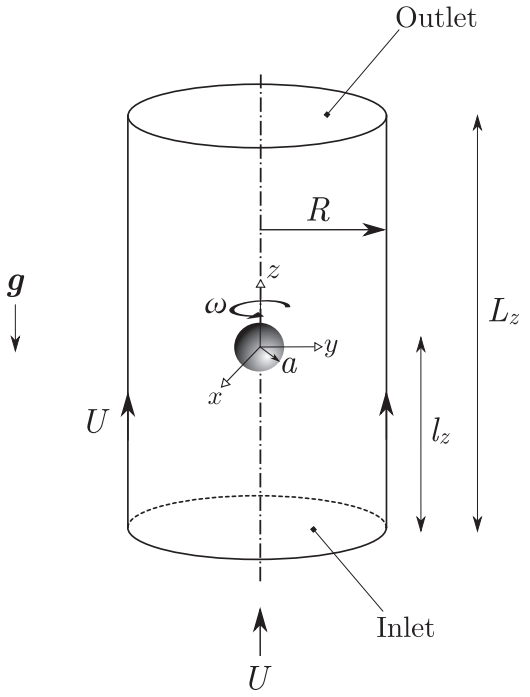

FIG. 3. Computational domain used for simulation.

dimensions using either cylindrical or spherical coordinates. Since this symmetry was not known *a priori*, we used a fully 3D code to numerically evaluate the equations described in Sec. III A.

For the comparison with the experiments, we solve the mobility problem, where the external force acting on the sphere (due to gravity) is specified and we determine the terminal settling speed (U) iteratively using the force acting on the sphere in the z direction, such that the hydrodynamic force balances the gravitational force acting on the sphere at steady state. All simulations were run for times of at least 20λ and $50a/U$. At steady state, the calculated hydrodynamic force on the sphere was within 0.0002% of the gravitational body force for all simulations.

For the comparison with the experiments, the computational domain was a tube of radius $R = 12.5a$ and length $L_z = 40a$, with a distance $l_z = 20a$ from the inlet to the sphere center. The mesh contained approximately 6.2 million elements, with smaller elements near the surface of the sphere of resolution $\Delta x = a/40$ to resolve the stress gradients accurately. A constant time step was chosen such that the bulk CFL (Courant–Friedrichs–Lewy) number in these simulations was $U\Delta t/\Delta x < 0.015$. A second, coarser mesh was used to test for mesh convergence. This second mesh had approximately 2.3 million tetrahedral elements, with the smallest elements near the sphere of resolution $\Delta x = a/20$. We found that results for the terminal settling velocity matched for the two meshes within 1.5% for all Wi.

C. Asymptotic theory for weak elastic effects

As a complement to the numerical simulations, for small values of Wi and De we solve the governing equations by a regular perturbation expansion. This perturbation theory is valid in the limit $\mathrm{De} \ll 1$ and $\mathrm{Wi} \ll 1$, implying that the elastic part of the fluid relaxes quickly relative to the rate at which it is deformed by the moving sphere and its rotation. The perturbation expansion is carried out in De and Wi, such that the highest-order terms considered in this expansion are $O(\mathrm{De}^2)$, $O(\mathrm{Wi}^2)$, and $O(\mathrm{WiDe})$. There are three important features of the asymptotic theory that should be

mentioned. First, the theory is valid for Re = 0, i.e., we neglect the effects of fluid inertia. Second, the theory is carried out for an unbounded domain. Third, in the theory, we model the viscoelastic stress tensor, σ_{ij}^{p}, with the Oldroyd-B constitutive equations [45,46,48]. These equations can be written by setting $\psi = 1$ in Eqs. (6) and (7).

In the theory, we solve the governing equations following the method of Einarsson and Mehlig [55], who solved the related mobility and resistance problems of a sphere settling in a linear flow. We adopt their Mathematica code [56], and the resulting notebook is available upon request.

The purpose of this asymptotic theory was twofold. First, we wanted to provide additional evidence that an observed change in the drag due to sphere rotation in a viscoelastic fluid was an elastic effect that would still be expected in weak elastic flows in the absence of fluid inertia. Additionally, by using the Oldroyd-B equation, we wanted to examine whether this change in the drag was observed in a fluid with a constant shear viscosity and a constant first normal stress coefficient in simple shear. Giesekus [34] theoretically predicted that, for a third-order fluid, a rotation imposed in the direction parallel to translation would reduce the drag on the sphere at $O(\mathrm{Wi}^2)$. The theory presented in this paper replicates that analysis using the Oldroyd-B constitutive equations. Second, the theory presented in this paper is used as a validation of our numerical solutions at small De and Wi.

Thus, to compare to the asymptotic theory, a set of numerical simulations were run using the methodology described in Sec. III B. To compare directly with the theory, we use the Oldroyd-B constitutive model to describe the polymer stress in this set of simulations. Additionally, in the momentum equation, we remove the convective term such that the solver is an unsteady Stokes solver, as has been done previously [54]. The computational domain used was a tube of radius $R = 20a$ and length $L_z = 40a$, with a distance $l_z = 20a$ from the inlet to the sphere center, as in Fig. 3. The mesh contained approximately 3.7 million tetrahedral elements, with smaller elements near the surface of the sphere of size $\Delta x = a/40$, and a bulk CFL number less than 0.0002. Since this set of simulations was used to compare to a theory valid for an unbounded domain, we verified that the change in the drag differs by less than 0.5% when the domain is increased by a factor of two, i.e., $R = 40a$, $L_z = 80a$, and $l_z = 40a$.

IV. EXPERIMENTAL RESULTS

To calculate the terminal velocity experimentally, five tests of each sphere, fluid, and rotation frequency combination were conducted to obtain a mean velocity. To calculate the experimental drag coefficient, we used the well-known equation:

$$C_d = \frac{8ag}{3U^2}\left(\frac{\rho_s}{\rho_f} - 1\right), \tag{9}$$

where U, ρ_s, ρ_f, g, and a correspond to the terminal settling speed, sphere density, fluid density, gravity, and sphere radius, respectively. Under creeping flow conditions, the Stokes settling speed is

$$U = \frac{2}{9}\frac{(\rho_s - \rho_f)ga^2}{\eta}, \tag{10}$$

where η is the fluid viscosity. For Newtonian experiments in creeping flow conditions, the drag coefficient then takes the form

$$C_d = \frac{24}{\mathrm{Re}}, \tag{11}$$

where the Reynolds number due to sedimentation is defined as

$$\mathrm{Re} = \frac{\rho_f U(2a)}{\eta}. \tag{12}$$

TABLE IV. Typical values of Wi and De (values of De are reported from the smallest sphere radius trial).

Frequency (Hz)	Wi	De ($D = 7.99$ mm)
0	0	1.93
0.83	2.67	1.96
1.67	5.34	1.93
2.50	8.01	1.92
3.33	10.69	2.02
4.17	13.36	2.19
5.00	16.03	2.35

Therefore, deviations with respect to the Newtonian case, for example, due to elastic fluid behavior, can be assessed by the normalized drag coefficient:

$$X_e = \frac{C_d \mathrm{Re}}{24} = \frac{F_d}{6\pi \eta a U}, \tag{13}$$

where F_d is the scalar hydrodynamic drag force on the sphere. At steady state, the hydrodynamic drag force is balanced by the external force on the sphere (F_{ext}), which in the case of a settling sphere is $F_{\mathrm{ext}} = F_g = 4\pi a^3(\rho_s - \rho_f)g/3$.

Due to the rotation of the sphere, we can also define a Reynolds number from sphere rotation as $\mathrm{Re}_\omega = \rho_f \omega a^2/\eta$, where ω is the rotation speed.

For our viscoelastic fluid flows, we can define a Deborah number and a Weissenberg number relating the characteristic polymer relaxation timescale with a characteristic flow timescale due to the translational and rotational motion, respectively. We can write the Deborah number, De, and a rotational Weissenberg number, Wi, as previously discussed:

$$\mathrm{De} = \frac{\lambda U}{a}, \tag{14}$$

$$\mathrm{Wi} = \lambda \omega, \tag{15}$$

where in this investigation, as discussed in Sec. II A, $\lambda = \lambda_{N_1}$ for experimental comparison. We differentiate between the Deborah and Weissenberg numbers in this study, unlike the previous study by Godinez *et al.* [36], since in viscoelastic fluids the modes of deformation from sphere translation and sphere rotation are characteristically different, particularly at finite values of the Deborah and Weissenberg numbers.

Values of the Deborah number were above one in the case without rotation and ranged from $1.93 < \mathrm{De}_{\mathrm{Wi}=0} < 2.35$. High values of Wi were reached due to the rotation, as this movement could lead to shear rates over 30 s^{-1}, resulting in rotational Weissenberg numbers that could exceed 10. For most of the rotation rates studied here, the flow around the sphere was rotation-dominated, i.e., $\mathrm{Wi} > \mathrm{De}$. Typical values of De and Wi in these experiments are shown in Table IV for one specific sphere diameter.

To compare the magnitude of the elastic and inertial effects, we can define an elasticity number, $\mathrm{El} = 2\mathrm{De}/\mathrm{Re} = \mathrm{Wi}/\mathrm{Re}_\omega = \lambda\eta_0/(\rho_f a^2)$. For all experiments and all spheres, $\mathrm{El} > 12$, suggesting these flows are dominated by elastic effects. The elasticity number can help distinguish between flows dominated by inertia or elasticity. For example, in the case of a purely rotating (nontranslating) sphere, as introduced in Sec. I, a secondary flow driven by inertial effects will move fluid toward the sphere near the poles at the axis of rotation and out along the equatorial plane where the centrifugal force is highest. In a viscoelastic fluid, when elastic effects dominate, the secondary flow is reversed and fluid moves toward the sphere along the equatorial plane and away from the sphere at the poles [45]. According to the analyses of Thomas and Walters [18], Walters and Savins [27], and

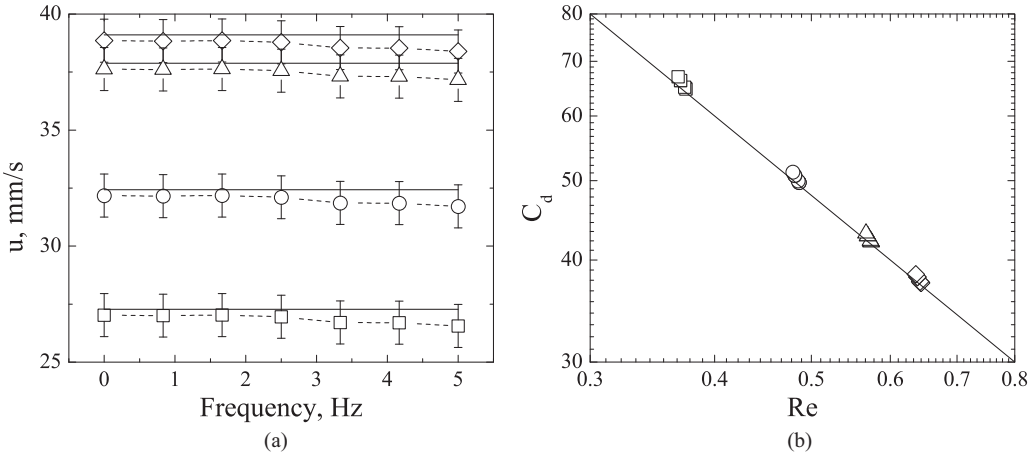

FIG. 4. (a) Terminal velocity u (mm/s) as a function of the frequency of rotation (Hz). Symbols refer to experimental measurements of the spheres with different diameter: 7.99 mm (squares), 8.72 mm (circles), 8.81 mm (triangles), and 9.57 mm (diamonds), whereas solid lines represent Stokes settling speed. (b) Comparison of drag coefficient data for the Newtonian fluid with Stokes law (solid line).

Manero and Mena [28], a viscoelastic parameter $m = (N_1 + 2N_2)/(2\rho_f a^2\dot{\gamma}^2)$ dictates the transitions between inertially and elastically driven secondary flows, where for $m > 1/4$, the secondary flow is predicted to be driven by elastic stresses. In our case, using Eqs. (1) and (2) for an Oldroyd-B fluid, we can see this viscoelastic parameter is related to the elasticity number by the polymer contribution to the viscosity as $m = \mathrm{El}(1-\beta)$, which is much greater than $1/4$ for all experiments. The elastic Mach number, defined as $\mathrm{Ma} = \sqrt{\frac{1}{2}\mathrm{DeRe}}$ [5,57], is less than 1 for all experiments.

First, to assess the experimental technique, a series of measurements were conducted in a Newtonian fluid. In Fig. 4(a), the terminal velocity of the sedimenting spheres is shown as a function of the rotation frequency. Clearly, the speed of sedimentation is unaffected by the rotation. The lines in the plot show the calculated Stokes settling speed according to Eq. (10). The agreement in all cases is within the experimental error (all error bars depict the standard deviation from the mean). The same data is presented in dimensionless terms in Fig. 4(b), where drag coefficient is shown as a function of the Reynolds number, and the drag coefficient is calculated from Eq. (9). Along with the measurements, the prediction of the drag for spheres, according to Eq. (11), is also shown. The agreement is remarkable and also shows that the rotation for a sphere sedimenting in a Newtonian fluid does not appear to cause any changes in the drag at these values of the Reynolds numbers.

The experimental measurements obtained for the Boger fluid are shown in Fig. 5, where the sedimentation velocity for the four spheres is plotted as a function of the rotation speed. In all cases, the sedimentation velocity is relatively constant at small rotation speeds, but tends to increase for larger rotation speed values. Fig. 5(b) shows the same data but in terms of the drag coefficient, again, calculated form Eq. (9), as a function of Reynolds number. Along with the experimental values of the drag coefficient, the Newtonian prediction is shown. Clearly, the drag for spheres sedimenting in this Boger fluid is significantly larger than the Newtonian value, even without rotation. Furthermore, when the rotation is applied, the drag is reduced significantly showing a decrease with Reynolds number which is, in fact, stronger than the Newtonian rate (approximately $\mathrm{Re}^{-1.5}$). The drag reduction is of up to 30% relative to the measurements without rotation.

Since the same measurement was conducted for the two different fluids, a direct comparison can be conducted. Note that the spheres are the same, sedimenting in fluids with approximately the same

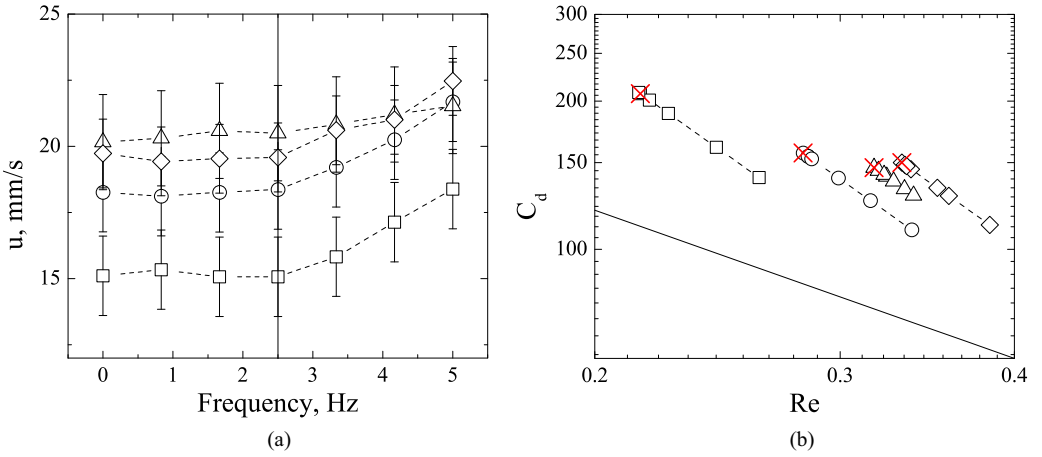

FIG. 5. (a) Terminal velocity u (mm/s) as a function of the frequency of rotation (Hz). Symbols refer to experimental measurements of the spheres with different diameter: 7.99 mm (squares), 8.72 mm (circles), 8.81 mm (triangles), and 9.57 mm (diamonds). (b) Comparison of drag coefficient data for the viscoelastic fluid with Stokes law (solid line); crossed out markers represent measurements without rotation.

value of viscosity, but the fluid densities are slightly different. Most importantly, one of the fluids is viscoelastic while the other one is Newtonian.

Figure 6(a) shows the drag coefficient as a function of Re, for all the measurements conducted in this study. The plot clearly shows the differences between the Newtonian and Boger fluid. It also demonstrates the effect of rotation on the drag coefficient. Two salient features can be readily identified: the drag is much larger in the Boger fluid; and when rotation is applied, a significant increase in the sedimentation velocity (and thus a clear reduction in the drag) occurs. The rotation-

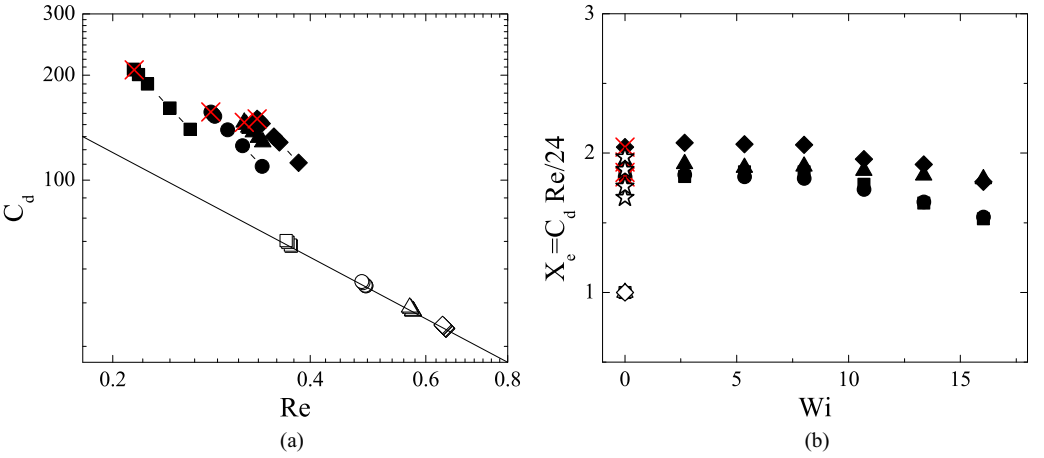

FIG. 6. (a) Comparison of drag coefficient data for the Newtonian (empty markers) and the Boger fluid (filled markers) with Stokes law (solid line). Symbols refer to experimental measurements of the spheres with different diameter: 7.99 mm (squares), 8.72 mm (circles), 8.81 mm (triangles), and 9.57 mm (diamonds). Crossed out markers represent measurements without rotation. (b) Dimensionless drag coefficient X_e as a function of the Weissenberg number Wi for the Newtonian (empty markers) and Boger fluid (filled markers). The symbols are the same as in (a) with the addition of the experimental measurements obtained by Ref. [6] (open stars).

driven drag reduction occurs at a slightly higher rate than that caused by an increase in Reynolds number for Newtonian fluids. This drag reduction is believed to be due to the elasticity of the polymeric Boger fluid. Note that, since the sedimentation speed is different for each of the fluids, both the values of the drag and Reynolds number change.

Figure 6(b) shows the normalized drag coefficient, defined in Eq. (13), for all the measurements in the Boger and Newtonian fluids, as a function of the rotational Weissenberg number calculated according to Eq. (15). The plot shows that for the case of the Boger fluid, the drag is about twice the Newtonian value when rotation is absent. Such values are in reasonable agreement with the measurements obtained by Jones *et al.* [6], who also used a corn syrup-based Boger fluid. When rotation is applied, the corrected drag coefficient is observed to clearly decrease with Weissenberg number.

As discussed at the beginning of this section, for a sphere rotating (but not translating) in a viscoelastic fluid, in a regime where the secondary flow is driven mainly by elastic stresses (as in these experiments), the fluid moves toward the sphere in the equatorial plane, and away from the sphere near the axis of rotation. On a physical basis, as the sphere rotates, polymers are stretched along the curved streamlines, adding tension to the streamlines and generating hoop stresses. This extra tension pulls fluid toward the sphere and away at the poles of rotation. For a sedimenting sphere, these rotation-induced hoop stresses are convected to the back of the sphere, providing a potential mechanism for an extra hydrodynamic force on the sphere, which could result in an enhanced settling velocity. This will be explored in the following section using numerical simulations.

V. NUMERICAL AND THEORETICAL RESULTS

Numerical simulations were used to compare with the experimental results and elucidate the effect of sphere rotation on the drag coefficient. First, in Sec. V A, we present the results of the asymptotic theory, compared with a set of numerical simulations for validation. Next, in Sec. V B, we present the results of the numerical simulations compared to the experiments, and propose a physical explanation for what is observed experimentally.

A. Asymptotic theory

In the perturbation theory, the calculation proceeds by assuming that the Deborah number $\mathrm{De} = \lambda U/a$ and Weissenberg number $\mathrm{Wi} = \lambda\omega$ are small, as described in Sec. III C. For the polymeric stress, we've chosen to use the Oldroyd-B constitutive model. From the theory, for a given value of De and Wi, we calculate the drag force (F_d) on the sphere. This is slightly different from the experiment where the external force on the sphere is fixed, and the terminal settling speed U is measured. However, both setups can be used to understand how the steady drag changes as a function of Wi, and here we will present results for the resistance setup (i.e., fixed U). The result for the drag, to second order in De and Wi, is

$$X_e = \frac{F_d}{6\pi\eta a U} = 1 - (1-\beta)\mathrm{De}^2\frac{258 + 143(1-\beta)}{25025} - (1-\beta)\mathrm{Wi}^2\frac{141 - 11(1-\beta)}{1155}. \tag{16}$$

The $O(\mathrm{De}^2)$ term in Eq. (16) is the first correction to the drag due to fluid elasticity (in the absence of sphere rotation) and matches what has been shown before [34,39,55,58], namely, a drag reduction for small De at $O(\mathrm{De}^2)$. Recently, a higher-order theory has shown that the drag can be significantly enhanced at higher De [59], in accordance with what was found experimentally in this study and elsewhere [3]. The $O(\mathrm{Wi}^2)$ term is the first correction to the drag due to sphere rotation in an elastic fluid, showing a drag reduction at small Wi. The scaling is the same as that found by Giesekus [34], although it should be noted that the coefficients are not precisely the same.

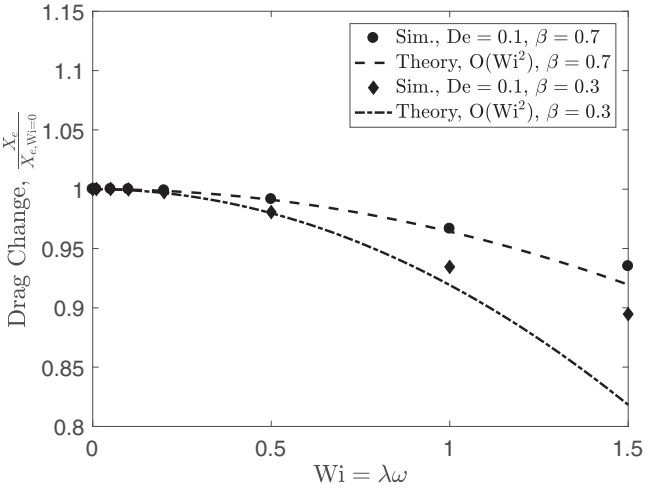

FIG. 7. Change in the normalized drag correction factor, X_e, as a function of the rotational Weissenberg number, $\mathrm{Wi} = \lambda\omega$. Shown is the comparison of the theory (lines) to the numerical solutions (symbols) for $\beta = \eta_s/\eta_0 = 0.3$ and $\beta = 0.7$ in an Oldroyd-B fluid.

A comparison between the simulation results and the theoretical result is shown in Fig. 7. In this plot, the drag correction factor (X_e) at a given rotational Weissenberg number is normalized by the drag correction factor at $\mathrm{Wi} = 0$. Two values for the solvent contribution to the viscosity were chosen, $\beta = 0.3$ and $\beta = 0.7$. In this set of simulations, the Oldroyd-B model was used for the polymeric stress to compare directly with the asymptotic calculations. The Deborah number was set to be $\mathrm{De} = 0.1$ and the drag force on the sphere was calculated. The simulations show good agreement with the theory (within 2%) for $\mathrm{Wi} \leqslant 1$.

B. Simulation results compared to experiments

To compare the simulations directly to the experiments, we used the fluid and sphere properties shown in Tables I–III. As discussed in Sec. III A, in this set of simulations we used the FENE-P constitutive model to describe the polymeric contribution to the Boger fluid stress. Starting with the relaxation time from Table II ($\lambda = 0.5102\,\mathrm{s}$), we fit the remaining FENE-P model parameters as $\eta_0 = 0.8644$ Pa s, $\beta = 0.2201$, and $L = 32.07$ using nonlinear regression to minimize the error between the FENE-P model and the steady-shear data (η and N_1) for $\dot{\gamma} \leqslant 20\ \mathrm{s}^{-1}$ from Fig. 1. The model fit is shown in Fig. 1. In our simulations, we chose to compare to a single experimental trial, where $d = 7.99$ mm and $\rho_s = 2190\,\mathrm{kg/m^3}$, and imposed a rotation rate on the sphere as given in Table IV. The sedimentation Reynolds number in the simulations, as defined in Eq. (12), ranged from $0.31 < \mathrm{Re} < 0.52$, similar to that from the experiments.

In Fig. 8, the change in the drag correction factor, X_e, is plotted as a function of rotational Weissenberg number, $\mathrm{Wi} = \lambda\omega$, from simulations and a single experimental trial. In this plot, we again plot $X_e/X_{e,\mathrm{Wi}=0}$; for the mobility setup (fixed F_{ext}) used in the experiments and these simulations, this is equivalent to plotting $U_{\mathrm{Wi}=0}/U$. From Fig. 8, we observe that the simulations do qualitatively capture the decrease in the drag coefficient (or increase in the settling velocity) as the rotation rate is increased.

The simulations fail to predict the large drag increase for the particle in the purely sedimenting (nonrotating) case at $\mathrm{Wi} = 0$, over-predicting $\mathrm{De}_{\mathrm{Wi}=0}$. From simulations, we calculated $\mathrm{De}_{\mathrm{Wi}=0} = 2.87$, whereas from the experiment, we measured $\mathrm{De}_{\mathrm{Wi}=0} = 1.93$. This corresponded to values of $X_{e,\mathrm{Wi}=0} = 1.22$ from the simulations and $X_{e,\mathrm{Wi}=0} = 1.86$ from the experiment; in other words, the drag on a purely sedimenting (nonrotating) sphere was underpredicted in the simulations. Possible

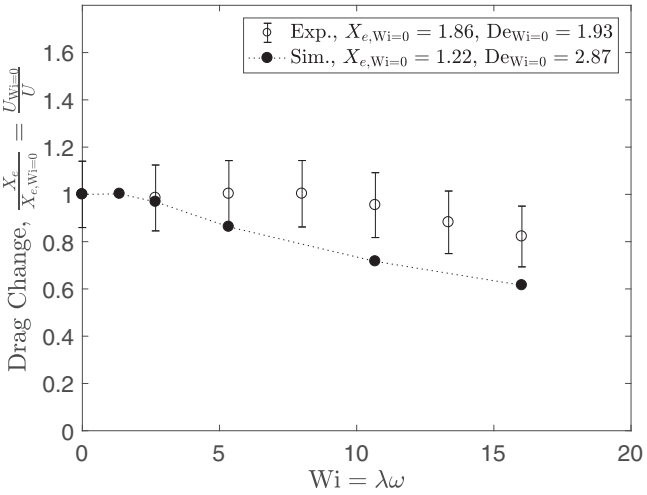

FIG. 8. Change in the normalized drag correction factor, X_e, as a function of the rotational Weissenberg number, $\mathrm{Wi} = \lambda\omega$. Results compare a single experimental trial ($d = 7.99$ mm), as open symbols, to numerical simulations, as closed symbols (a line is drawn through the numerical simulation data as a guide to the eye).

reasons for this discrepancy are addressed in Sec. III A, where we discuss the choice of the FENE-P constitutive model and the benefits and shortcomings of this model (and other dumbbell models) in complex flows. The value of $X_{e,\mathrm{Wi=0}}$ from our simulations is similar to that calculated by others using the FENE-P model [60] for similar values of $\mathrm{De}_{\mathrm{Wi=0}}$. In a more recent study, it was shown that inclusion of dissipative stress contributions can improve the quantitative description of the drag when using a modified hybrid FENE-CR and extensional White-Metzner model, although this construction adds an additional rheological parameter (a dissipative relaxation timescale) to the model [52]. To verify that the effect of rotation rate on the drag is not a strong function of $\mathrm{De}_{\mathrm{Wi=0}}$, we tested a second simulation case where the external force on the sphere was chosen such that the calculated terminal settling velocity in the absence of rotation matched that of the experiment (i.e., $\mathrm{De}_{\mathrm{Wi=0}} = 1.93$). With this reduced F_{ext}, we found that the change in the drag correction factor $X_e/X_{e,\mathrm{Wi=0}}$ in this second case was within 3% of the value shown in Fig. 8 at $\mathrm{Wi} = 5.3$. This conclusion seems to also be supported from the experimental measurements, where the effect of rotation rate on the drag does not appear to be a strong function of $\mathrm{De}_{\mathrm{Wi=0}}$, at least in the parameter range tested here.

Although the simulations qualitatively predict the decrease in the drag coefficient (or increase in the settling velocity) as the rotation rate is increased, the agreement is not quantitative at high Wi. It is possible that this discrepancy is partially explained by the limitations introduced by using the FENE-P model. Additionally, from the shear rheology plot in Fig. 1, we note that the Boger fluid used in the experiments appears to exhibit a slight increase in the shear viscosity for shear rates above 20 s^{-1} (i.e., $\mathrm{Wi} > 10$). This apparent thickening is not predicted by the FENE-P model (nor other dilute dumbbell models) and may further explain this discrepancy. Given the qualitative agreement and the possible explanations for the quantitative differences, we can therefore look to the simulations to explore the mechanism whereby the drag decreases for a rotating sphere in an elastic fluid.

In the simulations, we observed oscillations in the calculated terminal settling velocity at high values of the rotation Weissenberg number, $\mathrm{Wi} \geqslant 5.3$, which persisted even at long times (e.g., $t > 20\lambda$). The amplitude of these oscillations was approximately 2% at $\mathrm{Wi} = 5.3$ with a frequency of approximately $0.25/\lambda$. The amplitude grew to up to 10% at the highest tested $\mathrm{Wi} = 16.0$ with a frequency of approximately $0.4/\lambda$. The reported simulation values for $\mathrm{Wi} \geqslant 5.3$ are therefore averages over two periods of oscillations. We observed that the oscillation amplitude decreased

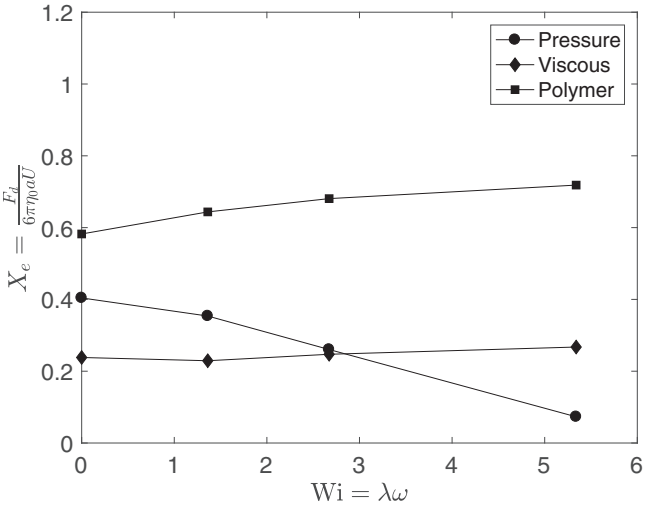

FIG. 9. Contributions to the drag correction factor, X_e, as a function of the rotational Weissenberg number, $\mathrm{Wi} = \lambda\omega$, from simulations.

approximately linearly as the CFL number was reduced, suggesting that the oscillations, if real, are small relative to the terminal settling velocity. The oscillation amplitude was not significantly changed when the computational domain was doubled in length. Previously, oscillations for a purely sedimenting (nonrotating) sphere have been observed in highly elastic fluids from both experiments [61] and numerical simulations [62,63], particularly in polymeric solutions with small viscous damping (i.e., small solvent contribution to the viscosity, β), as reviewed by McKinley [1].

C. Physical mechanism

From our simulations, we can compute the total drag force F_d experienced by the sphere by integrating the traction, $\sigma_{ij}n_j$, over the surface of the sphere. At steady state, this drag force is balanced by the gravitational body force on the sphere, $F_{\mathrm{ext}} = 4\pi a^3(\rho_s - \rho_f)g/3$. To further study the mechanism of the drag decrease due to sphere rotation, we can decompose the drag force into contributions from the pressure drag, viscous drag, and polymer drag. Thus, we can write the total drag (in the z or x_3 direction) at steady state as

$$X_e = \frac{F_d}{6\pi\eta_0 aU} = \frac{1}{6\pi}\left[-\int_S pn_3 dS + \beta\int_S\left(\frac{\partial u_3}{\partial x_k} + \frac{\partial u_k}{\partial x_3}\right)n_k dS + \int_S \sigma^P_{3k}n_k dS\right], \tag{17}$$

where the three terms above correspond to the pressure, viscous, and polymer drag, respectively. These contributions to the drag correction factor are plotted in Fig. 9 as a function of the rotational Weissenberg number. We observe that as the rotation rate is increased, the polymer drag on the sphere increases. However, this is outweighed by a strong decrease in the pressure drag experienced by the sphere. This reduction in the pressure drag is a notable result considering this is a low Reynolds number flow ($\mathrm{Re} < 1$) and suggests a change in the wake structure behind the sphere. This type of pressure-driven drag change in elastic fluids has been observed before, in both the purely sedimenting case [60], and in the case of a sphere settling in a cross shear flow [43], although in these two cases, the pressure drag drives an increase in the drag for highly elastic flows (i.e., for large De). It has also been observed that the dynamics of settling particles—including, e.g., lateral migration of a settling particle near a confining wall and interactions between two nearby settling particles—is affected by fluid viscoelasticity largely through a modification to the pressure distribution on the particles, rather than a direct contribution from the polymeric stresses [64]. The present case of the

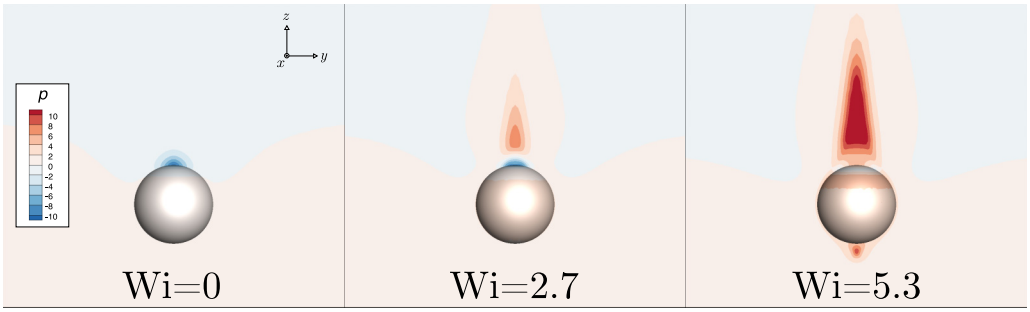

(a)

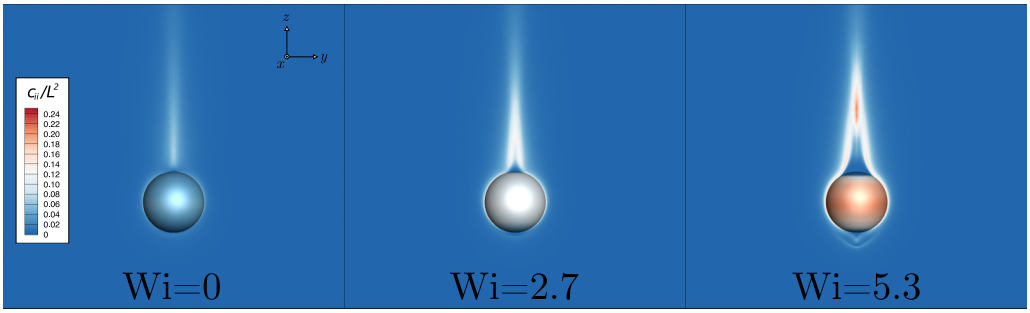

(b)

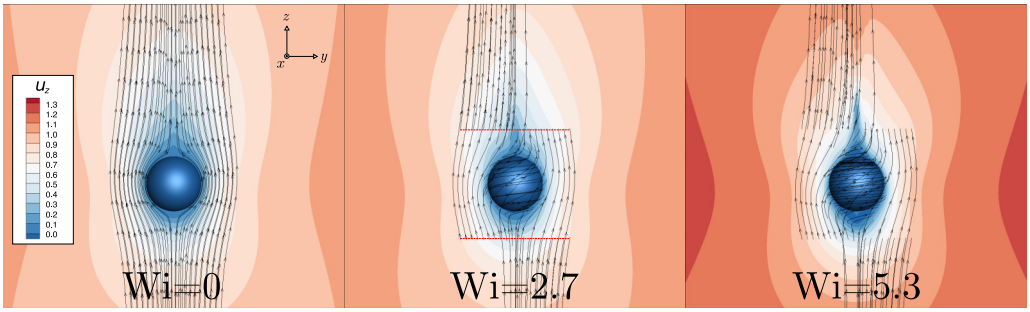

(c)

FIG. 10. (a) Pressure contours on the surface of the spherical particle and in the surrounding fluid (shown in the y-z plane). Pressure is minus the hydrostatic pressure and made dimensionless with $\eta_0 U_{\mathrm{Wi}=0}/a$. (b) Contours of the trace of the polymer conformation tensor normalized by the maximum polymer extensibility, c_{ii}/L^2, on the surface of the spherical particle and in the surrounding fluid (shown in the y-z plane). (c) Velocity contours of u_z, here made dimensionless with $U_{\mathrm{Wi}=0}$, on the surface of the spherical particle and in the surrounding fluid (shown in the y-z plane). Streamlines of (u_x, u_y, u_z) are seeded at $z = \pm 2$ and $x = 0$ across a range of y (seed lines are shown in red).

rotating and sedimenting sphere appears to be another example where the dominant viscoelastic effect appears indirectly as a modification of the pressure distribution experienced by the particle.

In Fig. 10(a), we show pressure contours on the surface of the particle and in the surrounding fluid at increasing rotational Weissenberg number. We can see that indeed the wake structure is significantly altered by the rotation of the sphere in this elastic fluid. As the rotational Weissenberg number is increased, a high-pressure region forms on the downstream side (in the wake) of the sphere. To investigate this, we examine the mechanism by which the polymers stretch in this flow.

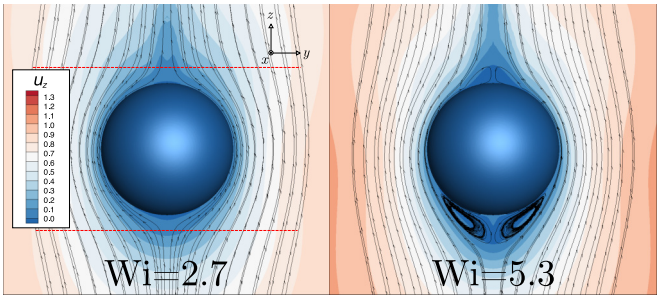

FIG. 11. Velocity contours, here made dimensionless with $U_{\mathrm{Wi}=0}$, on the surface of the spherical particle and in the surrounding fluid (shown in the y-z plane). Streamlines of $(0, u_y, u_z)$ are seeded at $z = \pm 1.25$ and $x = 0$ across a range of y (seed lines are shown in red).

In Fig. 10(b), we show the trace of the polymer conformation tensor, c_{ii}, on the surface of the particle and in the surrounding fluid. We observe that the polymers are highly stretched around the surface of the sphere as the rotational Weissenberg number increases. In Fig. 10(c), we show contours and streamlines of the velocity near the particle. We see that in the absence of rotation, fluid streamlines seeded in the y-z plane remain in that plane. As the rotation rate is increased, the fluid is rotated around the sphere in a three-dimensional envelope around the particle. We also note that in the downstream wake of the sphere, this wake envelope appears to be tightened at high rotational Weissenberg numbers.

As the rotational Weissenberg number increases, the polymers are stretched around the sphere, generating hoop stresses. These hoop stresses are then convected by the settling motion toward the downstream side of the sphere. We propose that these regions of high hoop stress induce an inward radial force that is balanced by the fluid pressure. This leads to the tightening of the wake and the high-pressure region that is observed in Fig. 10, resulting in a decrease in the pressure drag experienced by the sphere, and an increase in the particle settling velocity, as observed in the experiments.

In Fig. 11, we show a close-up of streamlines near the particle with the x component of the velocity set to zero. In doing so, we are able to visualize the start of a secondary flow at rotational Weissenberg numbers $\mathrm{Wi} \geqslant 5.3$, where we observe recirculation zones forming on the upstream side of the sphere. These secondary flows are reminiscent of those that have been observed previously for a rotating sphere viscometer in a viscoelastic fluid [27,29,30]. In the rotating-sedimenting case here, the recirculation zone forms as a result of the competition between the flow generated by the rotation of the sphere in the elastic fluid, which pulls fluid toward the sphere in the equatorial plane and out toward the poles, and the flow past the sphere.

The physical mechanism proposed here helps to illuminate why the drag decreases for a rotating sphere sedimenting in an elastic Boger fluid. This mechanism differs from that described for a sphere sedimenting and freely rotating in a cross sheared elastic Boger fluid, where the drag increases as the cross shear flow strength increases [40,41,43]. In the present case of the rotating sphere, the sphere is forced to rotate, e.g., due to an applied torque, in an otherwise quiescent fluid. For the parameter range explored here, this gives rise to azimuthal symmetry around the sphere's rotation axis. As described above, this results in the generation of hoop stresses as the sphere rotates, which are then convected toward the back of the sphere, leading to the formation of a high-pressure region on the back of the sphere and an overall decrease in the drag. In the latter case of the sphere in a cross shear flow, the sphere freely rotates due to the external flow, giving rise to 180° rotational symmetry about the sphere, with an azimuthally periodic variation in the traction (and the polymer stretch) near the sphere surface [65,66]. The external shear flow stretches polymers and generates tension along the shear flow streamlines, as well as convecting the stretched polymers near the sphere out into the shear flow direction. The extra fluid tension manifests as an increase in the drag

experienced by the sphere, and for a weakly elastic fluid flow past the sphere (i.e., De < 1) this becomes predominately a viscous drag increase at higher Wi [41,43]. For a highly elastic fluid flow past the sphere [i.e., De $\sim O(1)$] in a coupled cross shear flow, this sphere's wake region grows as the highly stretched polymers are convected into the shear flow direction to form viscoelastic "winglike" wake structures, deflecting flow past the sphere and resulting in predominately a pressure drag increase at higher Wi [43]. Although these mechanisms have important differences, it is possible that there exists a parameter regime where the effect of sphere rotation on the drag, from the present study, becomes important in the cross shear flow case, and this is an area for potential future investigation.

VI. CONCLUSIONS

In this study, we used a polyacrylamide/corn syrup Boger fluid to study the effect of viscoelasticity on the drag coefficient for a sedimenting and rotating sphere. In the purely sedimenting (nonrotating) case, we observed a drag coefficient that was larger than in a Newtonian fluid, in reasonable agreement with those obtained by Jones *et al.* [6], who also used a polyacrylamide/corn syrup-based Boger fluid. To study a simultaneously sedimenting and rotating sphere, we used a novel experimental setup to induce a controlled rotation of a sedimenting sphere about the axis aligned with gravity. We showed that with this setup, increasing the rotation rate of the sphere reduces the drag on the sphere in a viscoelastic fluid, resulting in an increased settling velocity. By using a nearly constant viscosity Boger fluid, it was demonstrated that this increase in the settling velocity is due to elastic effects. This result was supported by a perturbation theory for small De and Wi using an Oldroyd-B model, which showed that in the absence of fluid inertia, the drag is reduced at $O(\mathrm{Wi}^2)$. The experimental results were also supported by numerical simulations, which showed that the reduction in drag was likely attributable to convected hoop stresses from the rotating and translating sphere, which result in an increase in the fluid pressure on the backside of the sphere and an overall reduction in the drag. This finding suggests a possible mechanism for increasing the mobility of particles in viscoelastic fluids. We suggest that this conclusion would hold for active spherical particles as well, although this was not the focus of this study and deserves further investigation. A number of micro-organisms exhibit rotational motion during locomotion, for example mammalian spermatozoa, which have a rotating head driven by a rotating and beating flagellar tail, and *Volvox* colonies, which are roughly spherical squirmers that can rotate due to beating surface flagella [67,68]. Additionally, it seems likely that the change in the particle mobility is not only associated with the case where the rotation is around the axis aligned with translation, although alternate orientations were not studied here. For example, for a sphere translating and freely rotating in an external shear flow, an additional lateral drift has been predicted at $O(\mathrm{Wi})$ when the rotation is not aligned with the direction of translation [55,69,70]. Finally, as highlighted in Sec. I, the modifications in the drag coefficient for spheres settling in quiescent Boger fluids have been shown to be affected by the solvent quality and polymer extensibility in those fluids (which varies, e.g., between Type-I and Type-II Boger fluids). As such, in future investigations, it would be interesting to study how the related fluid rheological properties, such as the polymer extensibility parameter and the solvent contribution to the viscosity, affect the results presented here.

ACKNOWLEDGMENTS

A.C. acknowledges the support given by CONACYT-Mexico to pursue his graduate studies. J.E. thanks the Knut & Alice Wallenberg Foundation for their generous postdoctoral fellowship, Grant No. KAW 2015.0419. This material is based upon work supported by the National Science Foundation under Grants No. DGE-114747 (W.L.M.) and No. CBET-1337051, the US Army High Performance Computing Research Center, and the Stanford Certainty computer cluster, which is funded by the American Recovery and Reinvestment Act Grant No. W911NF07200271.

A.C. and W.L.M. contributed equally to this work.

[1] G. H. McKinley, Steady and transient motion of spherical particles in viscoelastic liquids, in *Transport Processes in Bubbles, Drops and Particles*, edited by D. De Kee and R. P. Chabra, 2nd ed. (CRC Press, Boca Raton, FL, 2002), chap. 14, pp. 338–375.
[2] B. Caswell, O. Manero, and B. Mena, Recent developments on the slow viscoelastic flow past spheres and bubbles, *Rheology Reviews*, edited by D. M. Binding and K. Walters (The British Society of Rheology, 2004), pp. 197–223.
[3] R. P. Chhabra, *Bubbles, Drops and Particles in Non-Newtonian Fluids*, 2nd ed. (CRC Press, Boca Raton, FL, 2006), chap. 5.
[4] G. D'Avino and P. L. Maffettone, Particle dynamics in viscoelastic liquids, J. Non-Newtonian Fluid Mech. **215**, 80 (2015).
[5] R. Zenit and J. J. Feng, Hydrodynamic interactions among bubbles, drops, and particles in non-Newtonian liquids, Annu. Rev. Fluid Mech. **50**, 505 (2018).
[6] W. M. Jones, A. H. Price, and K. Walters, The motion of a sphere falling under gravity in a constant-viscosity elastic liquid, J. Non-Newtonian Fluid Mech. **53**, 175 (1994).
[7] D. V. Boger, A highly elastic constant-viscosity fluid, J. Non-Newtonian Fluid Mech. **3**, 87 (1977).
[8] D. F. James, Boger fluids, Annu. Rev. Fluid Mech. **41**, 129 (2009).
[9] C. Chmielewski, K. L. Nichols, and K. Jayaraman, A comparison of the drag coefficients of spheres translating in corn-syrup-based and polybutene-based boger fluids, J. Non-Newtonian Fluid Mech. **35**, 37 (1990).
[10] M. Solomon and S. Muller, Flow past a sphere in polystyrene-based boger fluids: The effect on the drag coefficient of finite extensibility, solvent quality and polymer molecular weight, J. Non-Newtonian Fluid Mech. **62**, 81 (1996).
[11] D. Fabris, S. J. Muller, and D. Liepmann, Wake measurements for flow around a sphere in a viscoelastic fluid, Phys. Fluids **11**, 3599 (1999).
[12] V. Tirtaatmadja, P. H. T. Uhlherr, and T. Sridhar, Creeping motion of spheres in fluid m1, J. Non-Newtonian Fluid Mech. **35**, 327 (1990).
[13] M. T. Arigo, D. Rajagopalan, N. Shapley, and G. H. McKinley, The sedimentation of a sphere through an elastic fluid: Part 1. Steady motion, J. Non-Newtonian Fluid Mech. **60**, 225 (1995).
[14] K. Walters, *Rheometry* (Chapman and Hall, London, 1975).
[15] R. P. Chhabra, *Bubbles, Drops and Particles in Non-Newtonian Fluids*, 2nd ed. (CRC Press, Boca Raton, FL, 2006), chap. 11.
[16] K. Walters and N. D. Waters, On the use of a rotating sphere in the measurement of elastico-viscous parameters, Br. J. Appl. Phys. **14**, 667 (1963).
[17] K. Walters and N. D. Waters, The interpretation of experimental results obtained from a rotating-sphere elastoviscometer, Br. J. Appl. Phys. **15**, 989 (1964).
[18] R. H. Thomas and K. Walters, The motion of an elastico-viscous liquid due to a sphere rotating about its diameter, Q. J. Mech. Appl. Math. **17**, 39 (1964).
[19] H. Giesekus, Some secondary flow phenomena in general viscoelastic fluids, in *Proceedings of the 4th International Congress on Rheology*, edited by E. G. Lee (Brown University, Providence, RI, 1965), Vol. 1, pp. 249–266.
[20] R. A. Hermes, Measurement of the limiting viscosity with a rotating sphere viscometer, J. Appl. Polym. Sci. **10**, 1793 (1966).
[21] B. Mena, E. Levinson, and B. Caswell, Torque on a sphere inside a rotating cylinder, Z. Angew. Math. Phys. **23**, 173 (1972).
[22] R. A. Mashelkar, D. D. Kale, J. V. Kelkar, and J. Ulbrecht, Determination of material parameters of viscoelastic fluids by rotational nonviscometric flows, Chem. Eng. Sci. **27**, 973 (1972).
[23] J. V. Kelkar, R. A. Mashelkar, and J. Ulbrecht, A rotating sphere viscometer, J. Appl. Polym. Sci. **17**, 3069 (1973).
[24] A. Acharya and P. Maaskant, The measurement of the material parameters of viscoelastic fluids using a rotating sphere and rheogoniometer, Rheol. Acta **17**, 377 (1978).
[25] E. K. Cairncross and G. S. Hansford, An experimental investigation of the flow about a sphere rotating in a Rivlin-Ericksen fluid, J. Non-Newtonian Fluid Mech. **3**, 203 (1978).

[26] R. L. Fosdick and B. G. Kao, Steady flow of a simple fluid around a rotating sphere, Rheol. Acta **19**, 675 (1980).
[27] K. Walters and J. G. Savins, A rotating sphere viscometer, Trans. Soc. Rheol. **9**, 407 (1965).
[28] O. Manero and B. Mena, On the measurement of second normal stress using a rotating-sphere viscometer, Chem. Eng. J. **15**, 159 (1978).
[29] H. Giesekus, Stoff- und wärmeübertragung beim strömen schwach viskoelastischer flüssigkeiten um eine rotierende kugel, Rheol. Acta **9**, 30 (1970).
[30] I. E. Garduño, H. R. Tamaddon-Jahromi, and M. F. Webster, Oldroyd-B numerical simulations about a rotating sphere at low Reynolds number, Rheol. Acta **54**, 235 (2015).
[31] I. E. Garduño, H. R. Tamaddon-Jahromi, K. Walters, and M. F. Webster, The interpretation of a long-standing rheological flow problem using computation rheology and a PTT constitutive model, J. Non-Newtonian Fluid Mech. **233**, 27 (2016).
[32] I. E. Garduño, H. R. Tamaddon-Jahromi, and M. F. Webster, Shear-thinning and constant viscosity predictions for rotating sphere flows, Mech. Time-Depend. Mater. **20**, 95 (2016).
[33] O. S. Pak, L. Zhu, L. Brandt, and E. Lauga, Micropropulsion and microrheology in complex fluids via symmetry breaking, Phys. Fluids **24**, 103102 (2012).
[34] H. Giesekus, Die simultane translations-und rotationsbewegung einer kugel in einer elastoviskosen flüssigkeit, Rheol. Acta **3**, 59 (1963).
[35] R. K. Bhatnagar, Slow viscoelastic fluid flow past a rotating sphere, Int. J. Eng. Sci. **12**, 721 (1974).
[36] F. A. Godínez, E. de la Calleja, E. Lauga, and R. Zenit, Sedimentation of a rotating sphere in a power-law fluid, J. Non-Newtonian Fluid Mech. **213**, 27 (2014).
[37] J. R. Bourne, Further relationships for rotating sphere viscometers, Br. J. Appl. Phys. **16**, 1411 (1965).
[38] B. H. A. A. van den Brule and G. Gheissary, Effects of fluids elasticity on the static and dynamic settling of a spherical particle, J. Non-Newtonian Fluid Mech. **49**, 123 (1993).
[39] K. D. Housiadas and R. I. Tanner, The drag of a freely sedimentating sphere in a sheared weakly viscoelastic fluid, J. Non-Newtonian Fluid Mech. **183-184**, 52 (2012).
[40] R. I. Tanner, K. D. Housiadas, and F. Qi, Mechanism of drag increase on spheres in viscoelastic cross-shear flows, J. Non-Newtonian Fluid Mech. **203**, 51 (2014).
[41] S. Padhy, E. S. G. Shaqfeh, G. Iaccarino, J. F. Morris, and N. Tonmukayakul, Simulations of a sphere sedimenting in a viscoelastic fluid with cross shear flow, J. Non-Newtonian Fluid Mech. **197**, 48 (2013).
[42] S. Padhy, M. Rodriguez, E. S. G. Shaqfeh, G. Iaccarino, J. F. Morris, and N. Tonmukayakul, The effect of shear thinning and walls on the sedimentation of a sphere in an elastic fluid under orthogonal shear, J. Non-Newtonian Fluid Mech. **201**, 120 (2013).
[43] W. L. Murch, S. Krishnan, E. S. G. Shaqfeh, and G. Iaccarino, Growth of viscoelastic wings and the reduction of particle mobility in a viscoelastic shear flow, Phys. Rev. Fluids **2**, 103302 (2017).
[44] D. V. Boger and M. E. Mackay, Continuum and molecular interpretation of ideal elastic fluids, J. Non-Newtonian Fluid Mech. **41**, 133 (1991).
[45] R. B. Bird, R. C. Armstrong, and O. Hassager, *Dynamics of Polymeric Liquids*, Vol. 1: Fluid Mechanics, 2nd ed. (Wiley-Interscience, New York, 1987).
[46] R. B. Bird, C. F. Curtiss, R. C. Armstrong, and O. Hassager, *Dynamics of Polymeric Liquids*, Vol. 2: Kinetic Theory, 2nd ed. (Wiley-Interscience, New York, 1987).
[47] F. A. Godínez, O. Chávez, and R. Zenit, Note: Design of a novel rotating magnetic field device, Rev. Sci. Instrum. **83**, 066109 (2012).
[48] R. G. Larson, *Constitutive Equations for Polymer Melts and Solutions* (Butterworth-Heinemann, Oxford, UK, 1988).
[49] D. Richter, G. Iaccarino, and E. S. G. Shaqfeh, Simulations of three-dimensional viscoelastic flows past a circular cylinder at moderate Reynolds numbers, J. Fluid Mech. **651**, 415 (2010).
[50] M. Bajaj, M. Pasquali, and J. R. Prakash, Coil-stretch transition and the breakdown of computations for viscoelastic fluid flow around a confined cylinder, J. Rheol. **52**, 197 (2008).
[51] A. Abedijaberi and B. Khomami, Sedimentation of a sphere in a viscoelastic fluid: A multiscale simulation approach, J. Fluid Mech. **694**, 78 (2012).

[52] I. E. Garduño, H. R. Tamaddon-Jahromi, and M. F. Webster, The falling sphere problem and capturing enhanced drag with Boger fluids, J. Non-Newtonian Fluid Mech. **231**, 26 (2016).
[53] M. Yang, S. Krishnan, and E. S. G. Shaqfeh, Numerical simulations of the rheology of suspensions of rigid spheres at low volume fraction in a viscoelastic fluid under shear, J. Non-Newtonian Fluid Mech. **234**, 51 (2016).
[54] J. Einarsson, M. Yang, and E. S. G. Shaqfeh, Einstein viscosity with fluid elasticity, Phys. Rev. Fluids **3**, 013301 (2018).
[55] J. Einarsson and B. Mehlig, Spherical particle sedimenting in weakly viscoelastic shear flow, Phys. Rev. Fluids **2**, 063301 (2017).
[56] J. Einarsson, Computer algebra for microhydrodynamics, arXiv:1708.05788.
[57] D. D. Joseph, *Fluid Dynamics of Viscoelastic Fluids* (Springer-Verlag, Berlin, 1990).
[58] F. M. Leslie and R. I. Tanner, The slow flow of a visco-elastic liquid past a sphere, Q. J. Mech. Appl. Math. **14**, 36 (1961).
[59] K. D. Housiadas and R. I. Tanner, A high-order perturbation solution for the steady sedimentation of a sphere in a viscoelastic fluid, J. Non-Newtonian Fluid Mech. **233**, 166 (2016).
[60] B. Yang and B. Khomami, Simulations of sedimentation of a sphere in a viscoelastic fluid using molecular based constitutive models, J. Non-Newtonian Fluid Mech. **82**, 429 (1999).
[61] M. T. Arigo and G. H. McKinley, The effects of viscoelasticity on the transient motion of a sphere in a shear-thinning fluid, J. Rheol. **41**, 103 (1997).
[62] C. Bodart and M. J. Crochet, The time-dependent flow of a viscoelastic fluid around a sphere, J. Non-Newtonian Fluid Mech. **54**, 303 (1994).
[63] R. Zheng and N. Phan-Thien, A boundary element simulation of the unsteady motion of a sphere in a cylindrical tube containing a viscoelastic fluid, Rheol. Acta **31**, 323 (1992).
[64] J. Feng, P. Y. Huang, and D. D. Joseph, Dynamic simulation of sedimentation of solid particles in an Oldroyd-B fluid, J. Non-Newtonian Fluid Mech. **63**, 63 (1996).
[65] F. Snijkers, G. D'Avino, P. L. Maffettone, F. Greco, M. A. Hulsen, and J. Vermant, Effect of viscoelasticity on the rotation of a sphere in shear flow, J. Non-Newtonian Fluid Mech. **166**, 363 (2011).
[66] M. Yang and E. S. G. Shaqfeh, Mechanism of shear thickening in suspensions of rigid spheres in Boger fluids. Part I: Dilute suspensions, J. Rheol. **62**, 1363 (2018).
[67] T. J. Pedley, D. R. Brumley, and R. E. Goldstein, Squirmers with swirl: A model for Volvox swimming, J. Fluid Mech. **798**, 165 (2016).
[68] I. Fouxon and Y. Or, Inertial self-propulsion of spherical microswimmers by rotation-translation coupling, Phys. Rev. Fluids **4**, 023101 (2019).
[69] P. Brunn, The slow motion of a sphere in a second-order fluid, Rheol. Acta **15**, 163 (1976); **16**, 324 (1977).
[70] R. Vishnampet and D. Saintillan, Concentration instability of sedimenting spheres in a second-order fluid, Phys. Fluids **24**, 073302 (2012).